Bright Ratiometric Fluorescent Thermometer in Spin Crossover Molecule Enables Visualization of Spin-State Equilibria

Binbin Wang[1], Joseph Kfoury[2], Julianna Oláh[2], Lifei Zou[3], Shufang Xue[1*], Yunnan Guo[1*], Yann Garcia[4]

[1]Department of Chemistry, Key Laboratory of Surface & Interface Science of Polymer Materials of Zhejiang Province, Zhejiang Sci-Tech University, Hangzhou 310018, China. E-mail: yunnanguo@zstu.edu.cn; sfxue@zstu.edu.cn

[2]Department of Inorganic and Analytical Chemistry, Budapest University of Technology and Economics, Budapest H-1111, Hungary

[3]Inner Mongolia Key Laboratory of Photoelectric Functional Materials, College of Chemistry and Life Science, Chifeng University, Chifeng 024000, China

[4]Institute of Condensed Matter and Nanosciences, Molecular Chemistry, Materials and Catalysis (IMCN/MOST), Université catholique de Louvain, Place L. Pasteur 1, Louvain-la-Neuve 1348, Belgium.

Abstract

Optically addressable molecular spins aim to tackle control and detection of weak magnetic moment when magnetic devices are scaled down to the single-molecule level. To achieve accurate readout of molecular spin states by adjacent luminescent probes, the molecular design must meet the stringent requirements of both high signal-to-noise ratio (SNR) and high sensitivity.

Here, we incorporated a naphthalimide-based ratiometric fluorescent (RF) probe with a donor–acceptor (D-A) structure into a spin crossover molecule. The probe features dual emission channels arising from both a locally excited (LE) state and an intramolecular charge-transfer (ICT) state. The thermochromism associated to spin crossover spectrally overlaps with the probe's RF bands, producing a reverse synergistic effect, achieving ratiometric fluorescent thermometer with 1.35% K^{-1} sensitivity and 66% fluorescence contrast. More importantly, the bright fluorescence thermochromism (~50% yield) throughout the entire spin crossover process, enabling visualization of spin-state equilibria with high SNR (>400) and detection resolution (0.0017) even at low concentrations of 10^{-4} M. This tuning of the single-fluorophore RF against spin crossover thermochromism provides a new design platform for accurate read-out of spin states of molecules.

Introduction

In recent decade, extensive efforts have focused on integrating fluorescence with spin crossover (SCO) to optically track spin-state transitions at the molecular level.[1-3]

Compared to conventional SCO techniques such as magnetometry,[4] absorption spectroscopy,[5-6] and Mössbauer analysis,[7] luminescence detection offers superior sensitivity, simplicity and suitability for miniaturized or remote sensing.[8] Various SCO–fluorophore systems have been developed, including intensity-based,[9-12] wavelength-shift-based,[13-15] and ratiometric spin-state sensors.[16] Recently, these hybrid systems—featuring lanthanide-based luminophores such as Eu(III)[17] for red emission and Nd(III)[18] for near-infrared (NIR) emission—have demonstrated excellent quantitative correlations between the Fe(II) spin state and the corresponding emission outputs.

However, achieving effective fluorescent visualization of spin-state equilibria remains challenging, primarily because fluorescence is readily quenched by both/ether SCO-dependent FRET[10, 19] and/or thermally activated nonradiative decay of the luminophore.[20-21] These processes typically result in only weak emission fluctuations, rather than distinct signal switching or pronounced enhancement upon spin transition. In the solid state, this challenge is further intensified by aggregation-caused quenching (ACQ),[22-23] which severely diminishes emission intensity and often restricts detection to a qualitative level. Consequently, the overall signal-to-noise ratio (SNR>100[24]) and resolution (temperature uncertainty δT < 0.3 K[25]) are compromised—effectively trading strong fluorescence output for subtle spin-state information.

Compared to conventional single-channel fluorescent probes, ratiometric fluorescent probes offer significant advantages in dynamic sensing applications.[26-28] By employing two emission channels that vary in opposite directions, they amplify optical contrast[29] and provide a built-in self-referencing mechanism.[30-31] This dual-channel output significantly improves the resolution, and ensures more robust and reliable detection. Moreover, the accompanying fluorescence color change (i.e. fluorochromism[32] or ratiometric chromism[33]) enables intuitive visual identification and facilitates image-based sensing and data acquisition.[34-35]

In particular, recent advances in single-fluorophore ratiometric fluorescent probes have highlighted their potential for sensitive and quantitative detection of dynamic processes.[36] An effective design strategy is to construct donor–acceptor (D–A)-type

fluorophores that exhibit dual emission from both locally excited (LE) and intramolecular charge transfer (ICT) states.[37-38] Upon photoexcitation, temperature- or polarity-induced conformational changes[39-41]—such as planarization or twisting of the D–A bridge—enable interconversion between the LE and ICT states. As their relative emission intensities respond to external stimuli, a ratiometric fluorescence signal is generated,[42-44] allowing intuitive visualization and accurate monitoring of processes environmental perturbations.

In 2024, we reported an example of ratiometric fluorescence sensing of SCO using a naphthalimide-based ligand **L0** (Scheme S1),[16] which exhibited dual emission originating from the vibronic structure of the fluorophore. However, severe ACQ and strong Fe(II)-induced quenching rendered the optical visualization of spin-state equilibria functionally compromised. Here, building upon **L0**, we developed a single-fluorophore ligand **L1** (Scheme S1), in which a butylamino donor group is covalently tethered to a pyridine–triazole coordinating unit *via* naphthalimide fluorophore (Figure 1a). The introduction of the butylamino substituent not only markedly improves the solubility of **L1** in organic solvents but, more importantly, enhances the intramolecular D–A interaction. As a result, **L1** exhibits well-defined dual emission from both LE and ICT states (Figure 1b) as a bright single-fluorophore RF probe.

Building on this, we coordinated **L1** with Fe(II) to obtain a SCO Complex **1** (Figure 2a), which is structurally analogous to the well-established thermochromic complex $[Fe(abpt)_2(NCS)_2]$[45-47] (Figure 1d). The spectral overlap between the SCO-active Fe(II) center (Figure 1e) and the dual-emission of **L1** (Figure 1b) enables the thermochromic SCO transition to modulate the LE/ICT emission ratio, thereby achieving ratiometric fluorescence thermometry. Importantly, the high quantum yield of the thermochromic fluorescence in complex **1** allows for the optical visualization of spin-state equilibria.

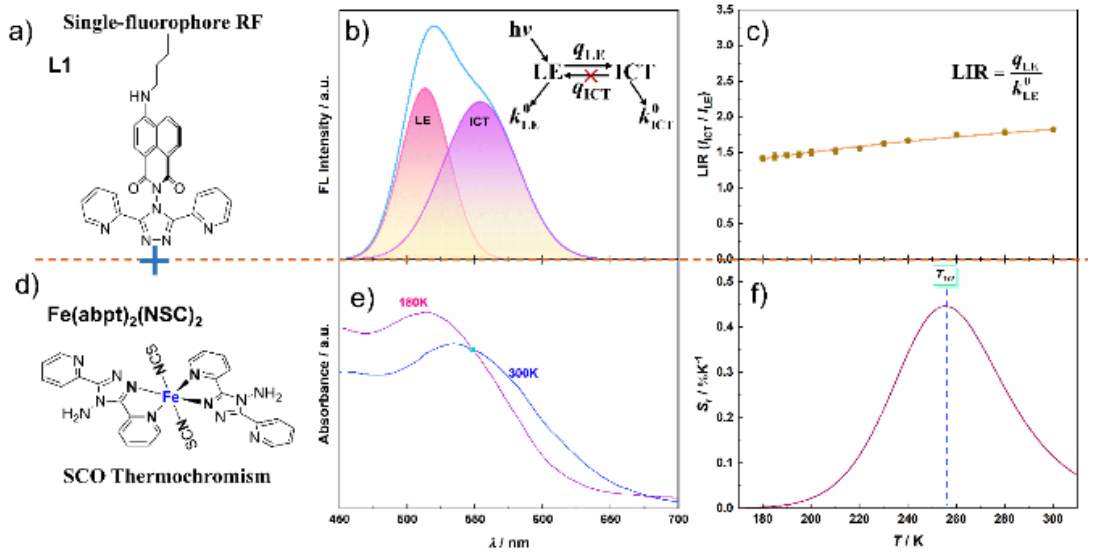

Figure 1. (a) The structural formula of the single-fluorophore RF ligand **L1**; (b) The dual emission behavior and mechanism of **L1**; (c) Luminescence intensity ratio (LIR) fitting of ligand **L1**; (d) The structural formula of SCO precursor [Fe(**abpt**)$_2$(NSC)$_2$];[45-47] (e) SCO Thermochromism of [Fe(**abpt**)$_2$(NSC)$_2$] at 180 K and 300 K and (f) sensitivity of [Fe(**abpt**)$_2$(NSC)$_2$] based on thermochromism ultraviolet absorption.

Result and discussion

Single-fluorophore Ratiometric fluorescence of L1

In THF solution, **L1** exhibits dual-emission bands centered at λ = 495 nm and λ = 550 nm in the temperature range of 180–300 K **(**Figure 1b and S1**)**. The stronger emission band at λ = 550 nm shows a pronounced Stokes shift that varies systematically with solvent polarity (Figure S2a,b). A linear Lippert–Mataga correlation (Figure S2c and Table S1)[48-49] confirms this dependence arises from a significant increase in the excited-state dipole moment, consistent with an ICT process.[50] The weaker emission at λ = 495 nm is attributed to a locally excited (LE) state, consistent with the emission of the naphthalimide unit in the unsubstituted analogue[16] and supported by theoretical calculations (Figure S3 and Figure S4).

Upon cooling, the two emission bands exhibit opposite intensity trends (Figure S5b), with the LE band increasing and the ICT band decreasing (Figure S6, Figure S7, Table S2) indicating a clear thermal coupling behavior between the two excited states. The Stevens–Ban plot of ln(Φ_{ICT}/Φ_{LE}) vs 1000/T [51] in Figure S5a reveals a linear relationship, consistent with the low-temperature limit described (section S2.1 in

detailed). From the slope of the linear fit, the activation energy for the LE → ICT transition, governed by the forward rate constant q_{LE} (Figure S8), is determined to be $\Delta E/k$ = 116 K (see Table S3 and insert of Figure 1b). In contrast, the absence of a high-temperature limit[52] up to 300 K indicates that the reverse process (ICT → LE) is negligible (i.e. $q_{ICT} \ll k^0_{ICT}$ as shown in eq. S17 and insert of Figure 1b). It is thereby deduced that LIR = q_{LE}/k^0_{LE} exhibits relatively weak intrinsic temperature dependence (eq. S18 and Figure 1c); nevertheless, this provides a stable baseline onto which SCO thermochromism can be externally integrated to modulate the fluorescence ratio (*vide infra*). Time-resolved fluorescence decays for both LE and ICT channels exhibit complete overlap (Figure S9a), indicating that their exponential decay rates are identical. This condition corresponds to $q_{LE} + k^0_{LE} = k^0_{ICT}$ (eq.S23). Therefore, the analytical solution for $k_{ICT}(t)$ allows direct estimation of the kinetic parameters in the scheme of Figure 1b: k^0_{ICT} = 0.16 ns^{-1}, k^0_{LE} =0.04 ns^{-1} and q^0_{LE} = 0.12 ns^{-1} (Table S3; see S2.2 in detailed).

The SCO precursor was synthesized following the reported method for [Fe(**abpt**)$_2$(NCS)$_2$] (abpt = 4-amino-3,5-bis(pyridin-2-yl)-1,2,4-triazole) (Figure 1d).[45] We initially focused on its thermochromic behavior in solution (Figure 1e). The relative sensitivity near ($T_{1/2}$) was found to be less than 0.5%/K (Figure 1f), indicating limited performance when used as a direct colorimetric temperature sensor. Nevertheless, as will be demonstrated later, when integrated as an external dual emission system based on **L1**, ratiometric fluorescent probes significantly amplifies the SCO response, highlighting its utility in hybrid thermometer responsive designs.

Structure and SCO of 1

Complex **1** was synthesized by a liquid–liquid diffusion method, in which a MeOH solution of $Fe(CF_3SO_3)_2 \cdot 6H_2O$ and NH_4SCN was carefully layered over a DCE solution of ligand **L1** (see section S1.1). Red-brown single crystals were obtained after slow diffusion. Single-crystal X-ray diffraction analysis at 100 K reveals that **1** is isostructural with its precursor complex[16](Table S4), with the molecular formula $Fe(\mathbf{L1})_2(NCS)_2 \cdot 2DCE$ (Figure 2a, space group *P*–1). The Fe(II) atom at inversion center, is coordinated by four nitrogen from two **L1** ligands (N4 and N5) and two nitrogen of terminal NCS^- anions (N7), arranged in a *trans*-dithiocyanato configuration (Figure S10). The six Fe–N bond distances range from 1.973(4) to 2.045(3) Å, and indicate a LS Fe(II) center (Table S5).

Due to the fragile nature and easy decomposition at elevated temperatures, its crystal structure in the HS state could not be determined by Single-crystal X-ray diffraction. However, magnetic susceptibility measurements (Figure S12a) revealed a $\chi_M T$ value of 3.124 $cm^3 \cdot K \cdot mol^{-1}$ at 300 K, as a fully HS state. Upon cooling, the $\chi_M T$ value gradually decreased to 0.763 at 100K before dropping to 0.286 at 5 K, indicating a typical one-step SCO with $T_{1/2}$ = 120(1) K.

The removal of two lattice DCE molecules, denoted as complex **1-d** (Figure S11 and S12b) induces cooperative spin transition at $T_{1/2}$ = 140(1) K with $n\Delta H$ = 18.8(4) kJ/mol, fitting by Domain model (Figure S12a). Cooperativity $n \approx 3$ was further estimated based on ΔH = 5.98(1) kJ/mol from differential scanning calorimetry (DSC) (Figure S12c).[16] This enhancement is attributed to the lattice contraction and tighter molecular packing caused by solvent loss, which strengthens intermolecular interactions and facilitates a more collective and cooperative spin-state switching.[53-54]

Thermochromism and ratiometric fluorescence performance in complex 1

The spin state of **1** in solution was evaluated using the Evans method[55] (eq. S1), which involves measuring the chemical shift change (Δf) of THF as the solvent in relation to the molar concentration of paramagnetic species (Figure S13, see section S1.4). A solution of $Fe(CF_3SO_3)_2 \cdot 6H_2O$ was used as a HS Fe(II) reference with linear dependence of Δf vs c (Figure 3a). Notably, complex **1** align closely with this calibration

line, indicating that it predominantly adopts a HS in THF solution at room temperature. To further investigate the thermal responsiveness of the spin state, temperature-dependent UV–vis absorption spectra were recorded (Figure 3b). Upon cooling to 180 K, a clear intensity redistribution between two absorption bands is observed on either side of the isosbestic point at λ = 528 nm, corresponding to the thermochromic shift in solution color (Inset of Figure 3b). This clear isosbestic point indicates a clean interconversion between two distinct species with a thermally driven two-state SCO process.

DFT and Time-Dependent DFT (TD-DFT) calculations assigned in both HS and LS configurations, the most intense absorption band centered at λ ~ 402 nm corresponds to a localized $\pi \rightarrow \pi^*$ transition within the naphthalimide group ($S_0 \rightarrow S_1$) (Figure S14a). In the LS state, an additional absorption band appears at λ = 534 nm, which is assigned to a metal-to-ligand charge transfer (^{1}MLCT) transition from d(Fe) + π(SCN) → π*(abpt) (Figure S14b). In contrast, the HS state exhibits a broader MLCT band centered around λ = 565 nm (^{5}MLCT), arising primarily from d(Fe) → π*(abpt) transitions and extending from λ = 389 to λ = 565 nm (Figure S14c,d). The thermal interconversion between these MLCT transitions underlies the reversible color change observed in solution. Similar phenomena have been reported in Fe(II) SCO systems containing 1,2,4-triazole–bipyridine ligands.[16]

Using eq.1, the thermodynamic parameters of the Fe(II) SCO process in solution were extracted (Figure 3c) with $T_{1/2} = \Delta H/\Delta S$= 250 K ($\Delta H$ = 15.5(2) kJ mol^{-1}, ΔS= 61.9(4) J mol^{-1} K^{-1}).[56]

$$\gamma_{HS}(T) = \frac{\varepsilon - \varepsilon_{LS}}{\varepsilon_{HS} - \varepsilon_{LS}} = \frac{1}{1 + e^{\Delta H/RT - \Delta S/R}} \quad (1)$$

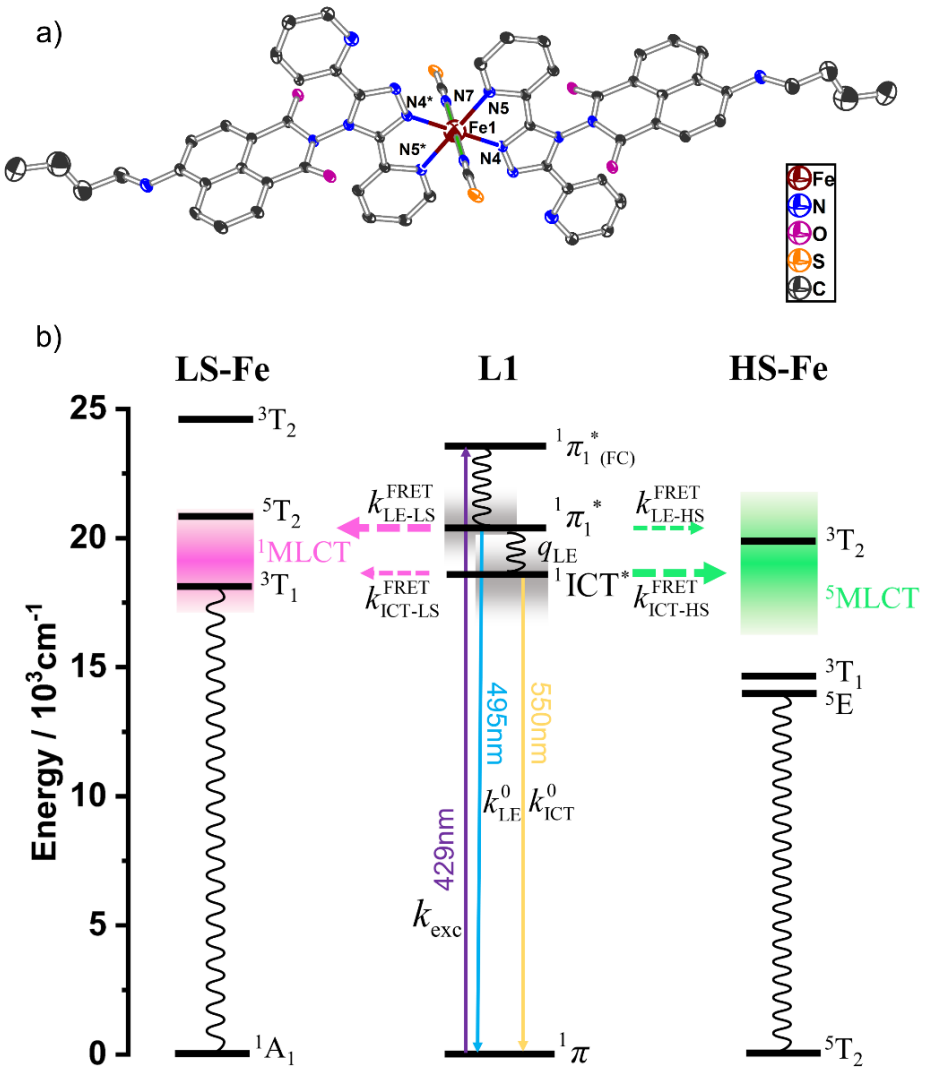

Figure 2. (a) Molecular structure of **1** at 100 K showing 20% probability of ellipsoids; hydrogen atoms are omitted for clarity. Symmetry code*: 2-*x*, 3-*y*, 2-*z*; (b) Jabłoński diagram summarizing the excitation processes (straight upward arrows), ETs (dashed arrows), nonradiative multiphonon relaxation (undulating arrows), and radiative emission processes (straight downward arrows) operating in LS-[Fe(**L1**)$_2$] and HS-[Fe(**L1**)$_2$].

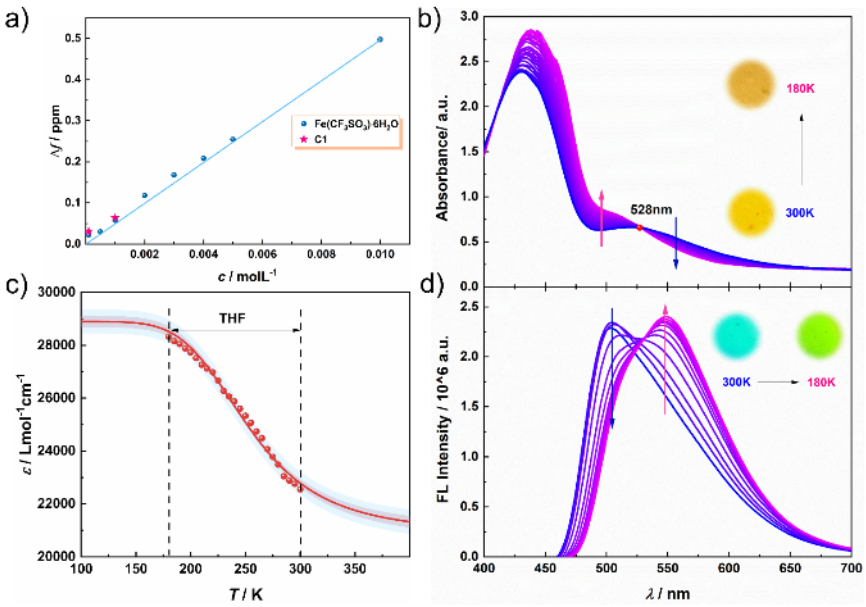

Figure 3. (a) ^{1}H NMR chemical shifts measured by the Evans method for $Fe(CF_3SO_3)_2 \cdot 6H_2O$ (blue dots) and complex **1** (pink dots) in THF solution; (b) Variable-temperature UV-Vis absorption spectra of **1** in THF (1.0×10^{-4} M, 180-300 K), (Inset: optical micrograph of **1** under ambient light at corresponding temperatures, Absorption Contrast: Abs_{495nm} = 32.09%; Abs_{550nm} = 26.20%); (c) Temperature-dependent absorbance of **1** at the characteristic wavelength λ = 441 nm (purple shaded area represents the confidence region of the fit, blue shaded area indicates the prediction region); (d) Variable-temperature fluorescence emission spectra of **1** in THF (1.0×10^{-4} M, 180-300 K), (Inset: fluorescence micrograph of **1** under UV irradiation at varying temperatures. Emission Contrast: PL_{495nm} = 65.92%; PL_{550nm} = 38.48%).

Complex **1** retains the intrinsic dual-emission characteristics of the free ligand, exhibiting two emission bands centered at λ = 495 nm and λ = 550 nm (Figure 3d, Figure S15, S16 and Table S6). Consistent with the ligand **L1**, complex **1** also exhibits ICT behavior (Figure S17, S18 and Table S7). However, in contrast to the ligand, complex **1** demonstrates a pronounced temperature-dependent evolution of these emission bands (Figure 4c) with a visible fluorescence color change (Figure 3d and S19). Such ratiometric fluorescence thermochromism is absent in the ligand alone, suggesting that strong thermal coupling is introduced upon coordination with Fe(II).

Although the incorporation of the Fe(II) center does not significantly perturb the ground-state electronic configuration of ligand **L1** (Figure S14a and Figure S3 left panel), it introduces new excited-state pathways—namely, spin-state-dependent ^{1}MLCT and ^{5}MLCT transitions—as well as additional metal-centered (MC) energy levels (Figure 2b) (The relevant energy level calculation diagram is shown in Figure S20). These MLCT states differ substantially between the LS and HS configurations. As a consequence, the broad absorption bands spanning λ = 450–650 nm in both LS

and HS states (Figure 4a and Figure S21) show significant spectral overlap with the LE and ICT emission bands of the ligand, providing the basis for Förster resonance energy transfer (FRET) (Table S8). The corresponding FRET rates can be calculated using the Förster theory according to eq. 2-3[57-58] where κ^2 is an orientation factor (Figure S22, S23 and Table S9. See section S1.6 in detail), N_A is the Avogadro constant in mmol^{-1}, n is the refractive index of the medium, k_D^0 is the radiative rate constant of the donor (Table S3), and $J_{D\text{-}A}$ is the normalized Förster spectral overlap integral in the wavenumber scale based on the definition of eq. 2[59]

$$J_{D\text{-}A} = \int_0^\infty \overline{F_D}(\lambda)\varepsilon_A(\lambda)\lambda^4 d(\lambda) \tag{2}$$

$$k_{FRET} = \frac{9\cdot\ln(10)}{128\cdot N_A\cdot\pi^5\cdot n^4}\cdot k_D^0\cdot\left(\frac{\kappa^2}{R^6}\right)\cdot J_{D-A} \tag{3}$$

We first inspected the $J_{D\text{-}A}$ between the donor (either LE or ICT states) and the acceptor (either ^{5}MLCT for HS or ^{5}MLCT for LS), which can be deduced four contributions of $J_{LE\text{-}LS}$ $J_{LE\text{-}HS}$ $J_{ICT\text{-}LS}$ and $J_{ICT\text{-}HS}$, (Figure 4b and FigureS19). For the LE emission channel, spectral overlap with Fe(II) absorption is stronger in the LS state due to the ^{1}MLCT band, leading to a larger $J_{LE\text{-}LS}$ than $J_{LE\text{-}HS}$ (top panels of Figure 4a). In contrast, for ICT emission, the broad ^{5}MLCT absorption band of the HS state exhibits nearly perfect spectral overlap with the ICT emission maximum (λ ~550 nm), resulting in a significantly enhanced $J_{ICT\text{-}LS}$ value compared to $J_{ICT\text{-}HS}$ ($J_{ICT\text{-}LS}$ <$J_{ICT\text{-}HS}$ in bottom panels, Figure 4a). Therefore, as shown in Figure 4b, the overall overlap integral between the ICT emission and Fe(II) absorption ($J_{ICT}^{D\text{-}A}$) increases with temperature, whereas that of the LE channel ($J_{LE}^{D\text{-}A}$) decreases, both evolving within the bounds defined by four asymptotic $J_{D\text{-}A}$ lines. This opposing trend directly correlates with the temperature-dependent fluorescence intensity changes shown in Figure 4c, reflecting an inverse relationship: the larger the spectral overlap, the weaker the emission, and *vice versa*.

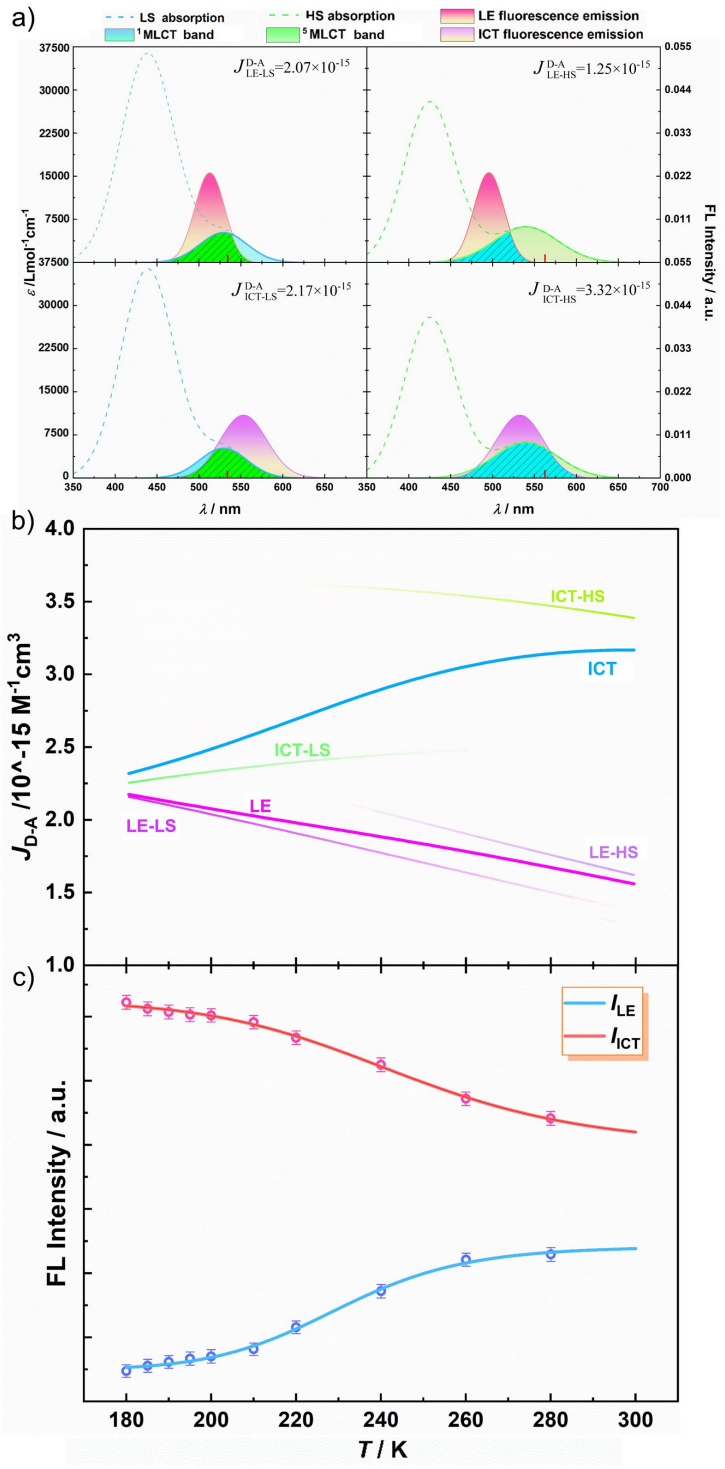

Figure 4. Normalized dual-emission fluorescence spectra of ligand **L1** overlapped with the UV-vis absorption spectra of complex **1**; (b) Temperature dependence of the spectral overlap integral areas derived from (a), (where $J^{D\text{-}A}_{LE}$ and $J^{D\text{-}A}_{ICT}$ are affected by the proportion of high spin in the SCO state. The temperature-dependent overall overlap integrals were calculated using a weighted average of HS and LS contributions: $J^{D\text{-}A}_{LE}(T)=\gamma_{HS}(T)\cdot J^{D\text{-}A}_{LE\text{-}HS}+\gamma_{LS}(T)\cdot J^{D\text{-}A}_{LE\text{-}LS}$ and $J^{D\text{-}A}_{ICT}(T)=\gamma_{HS}(T)\cdot J^{D\text{-}A}_{ICT\text{-}HS}+\gamma_{LS}(T)\cdot J^{D\text{-}A}_{ICT\text{-}LS}$, $\gamma_{HS}(T)$ and $\gamma_{LS}(T)$ represent the fractional population of high-spin and low-spin states at a given temperature, derived from UV-vis measurements). (c) Integrated intensities of photoluminescence at I_{LE} and I_{ICT} of **1**. Solid line was fitted by eq. 4, respectively, based on the parameters listed in Table 1 and S3.

To quantitatively describe the temperature-dependent fluorescence behavior of complex **1**, we constructed a steady-state emission model based on the energy level diagram shown in Figure 2b. In this diagram, the LE and ICT states undergo radiative decay as well as FRET to Fe(II)-centered MLCT in either LS or HS configurations ($k_{\text{LE-LS}}^{\text{FRET}}$,$k_{\text{LE-HS}}^{\text{FRET}}$,$k_{\text{ICT-LS}}^{\text{FRET}}$,$k_{\text{ICT-HS}}^{\text{FRET}}$) (Table S8 and Figure S24a,b). Assuming that SCO transitions are significantly slower than both radiative and FRET decay channels (10^{-6}s^{-1})[60-62], the LS and HS states are treated as thermally fixed subpopulations during the fluorescence lifetime (Figure S25). The total fluorescence intensities from the LE and ICT states at a given temperature are expressed as follows (section S2.3 in detail):

$$I_{\text{LE}} = \sum_{i=\text{HS, LS}} \frac{k_{\text{LE}}^{0}}{k_{\text{LE}i}} \cdot \gamma_i N_0 k_{\text{exc}}\,; \quad I_{\text{ICT}} = \sum_{i=\text{HS, LS}} \frac{q_{\text{LE}}}{k_{\text{LE}i}} \cdot \frac{k_{\text{ICT}}^{0}}{k_{\text{ICT}i}} \cdot \gamma_i N_0 k_{\text{exc}} \tag{4}$$

Here, $k_{\text{LE}i}=k_{\text{LE}}^{0}+k_{\text{LE}i}^{\text{FRET}}+q_{\text{LE}}$;$k_{\text{ICT}i}=k_{\text{ICT}}^{0}+k_{\text{ICT}i}^{\text{FRET}}$; γ_i refers eq. 1(Figure S8b) and k^{FRET} refers eq. 2-3. In this modeling process, the donor–acceptor geometric factor κ^2/R^6 in eq. 3 was treated as the only adjustable fitting parameter. All other physical quantities, $J_{\text{D-A}}(T)$ (Figure 4b), k_{D}^{0} and $q_{\text{LE}}(T)$ (Table S3 and Figure S8a), were independently determined from experimental data. Finally, the integrated emission intensities $I_{\text{LE}}(T)$ and $I_{\text{ICT}}(T)$ (obtained from Gaussian deconvolution, Figure S15) was performed using nonlinear least-squares fitting, and excellent agreement with the experimental data was achieved (Figure 4c). The full set of fitting parameters is compiled in Table 1.

Finally, four temperature-dependent FRET rate constants $k^{\text{FRET}}(T)$ were quantitatively extracted as shown in Figure S24a,b and Table 1. It is evident that $k_{\text{LE}}^{\text{FRET}}$ is significantly higher in LS state than in the HS state, whereas $k_{\text{ICT}}^{\text{FRET}}$ exhibits the opposite trend. In particular, this phenomenon is clearly reflected in the transient fluorescence experiments: a more than elevenfold difference between $k_{\text{ICT}\rightarrow\text{HS}}^{\text{FRET}}$ and $k_{\text{ICT}\rightarrow\text{LS}}^{\text{FRET}}$ is manifested in the ICT emission lifetime, which markedly increases upon cooling (Figure S25)—an effect that is absent in the free ligand system (Figure S9c,d). Collectively, these results indicate that the LE and ICT emission channels are more susceptible to FRET quenching at low and high temperatures, respectively. The

opposing temperature dependencies of the two channels constitute the fundamental driving force for the temperature-responsive ratiometric fluorescence.

Based on DFT-optimized geometries (Figure S23) and fitted κ^2/R^6 values in eq. 3 (Table 1), the estimated FRET distance is approximately 9.6 Å (Figure S22c), which matches the spatial separation between the Fe(II) center and the naphthalimide fluorophore (Figure S22c illustration). This spatially rationalized, relative low-efficiency FRET pathway not only enabling a sensitive and quantitative optical readout of the SCO process, but also, conversely, offering functional advantages for using SCO behavior to achieve enhanced performance in RFT. **The moderate FRET-induced quenching efficiency observed in 1 (33%–5% for LE and 4.2%–34% for ICT, see Figure S24c,d and Table 1) indicates a more favorable trade-off between fluorescence retention and spin-state sensitivity, allowing for efficient ratiometric readout without complete signal loss.** As a result, the complex maintains a high fluorescence quantum yield between 51% (LS) and 47% (HS) and sufficient emission intensity for reliable detection.

Table 1. Fitting data of fluorescence intensity of **1**

	LS (180 K)	HS (300 K)
$\kappa^2_{LE}/\overline{R}^6$ (Å^{-6})	2.93(3)·10^{-6}	4.68(4) 10^{-7}
$\kappa^2_{ICT}/\overline{R}^6$ (Å^{-6})	7.18(1) 10^{-8}	4.43(1) 10^{-7}
κ^2_{LE} (DFT)	1.92	1.08
κ^2_{ICT} (DFT)	0.24	0.47
$\overline{R}$/ Å	9.64	
k^{FRET}_{LE}/ ns^{-1} [a]	0.068(7)	0.008(5)
k^{FRET}_{ICT}/ ns^{-1} [a]	0.007(6)	0.081(7)
η^{ET}_{LE} / % [b]	32.7(1)	4.8(2)
η^{ET}_{ICT} /% [b]	4.2(1)	33.6(1)

Φ_{flu} /% [c]	51.3(2)	46.7(1)
Φ_{LE}/Φ_{ICT}	0.36	0.52

[a] The non-radiative transition rate of a LE ICT state. [b] $\eta_{LE}^{ET}=\frac{k_{LE}^{FRET}}{k_{LE}^{FRET}+k_{LE}^{0}+q_{LE}}\times100\%$, $\eta_{ICT}^{ET}=\frac{k_{ICT}^{FRET}}{k_{ICT}^{FRET}+k_{ICT}^{0}}\times100\%$. [c] The relative yield obtained based on the area ratio of **L1** to **1**.

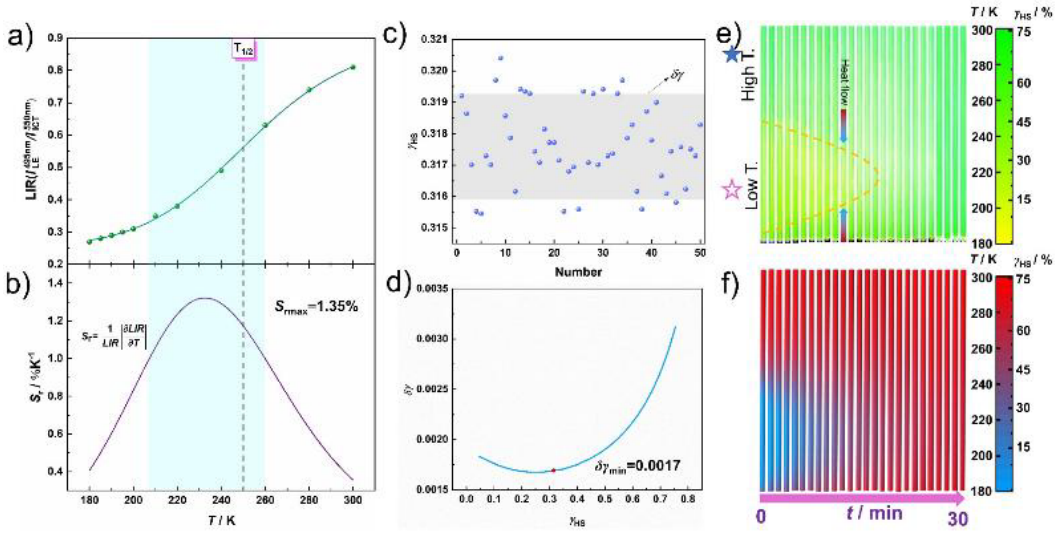

Figure 5. (a, b) LIR of complex **1** and its corresponding relative temperature sensitivity S_r; (c) Distribution of the high-spin state fraction (γ_{HS}) extracted from sequentially recorded spectra (n = 50) at selected temperatures; (d) Experimentally determined uncertainty in the spin state fraction ($\delta\gamma$) derived from the data in (c) (red dots); the blue line represents the theoretically calculated uncertainty using eq. S10 without any fitting parameters; (e) SCO process under dynamic thermal conduction within an NMR tube. Upper segment: 300 K (hot end); Lower segment: 210 K (cold end). After removal of the cold end, heat conducts from the room-temperature end (300 K) towards the center (as indicated by arrows); (f) Simulation of the temporal evolution of the temperature profile for the thermal conduction process depicted in (e), performed using COMSOL Multiphysics software.

Ratiometric Thermometric Performance and Visualization of Spin-State Equilibria

The SCO thermochromism induces a pronounced redistribution between LE and ICT emission intensities, enabling temperature to be optically diagnosed *via* spin-state-dependent dual emission. The relative thermal sensitivity S_r, $S_r=\left|\frac{1}{LIR}\cdot\frac{dLIR}{dT}\right|$, reaches a maximum of 1.35% K^{-1} near 230 K—just below the $T_{1/2}$, with temperature range of 210–260 K for $S_r > 1.0\%$ K^{-1}. The sensitivity markedly outperforms both the ICT-driven response of free **L1** (Figure S26) and the modest thermochromic shift observed in the SCO precursor [Fe(**abpt**)$_2$(NCS)$_2$] (Figure 1f). This highlights the amplified ratiometric fluorescence response enabled by the synergistic coupling of the dual-channel

fluorophore with SCO switching in complex **1**. **To the best of our knowledge, 1 represents the first single-molecule ratiometric fluorescent thermometer (RFT) that operates based on a spin state switching.**[8]

Owing to the Boltzmann-type dependence of the high-spin mole fraction $\gamma_{HS}(T)$ on temperature as shown in eq.1, the RFT enables a read-out of the spin-state equilibria. Figure 5c shows the temperatures that we extracted from a series of spectra using the calibration of Figure 5a. These values are evenly distributed around the mean, which is a sign of a stable physical temperature during the measurement. Using the method presented in Figure S27 (For details, see section S1.7), we determine the γ_{HS} resolution at various physical temperatures and find The minimum resolution of $\delta\gamma$ = 0.168 % (Figure S28) values of at γ = 0.323 (227.6 K) (Figure 5d and Figure S29), highlighting the remarkable precision of complex **1** in differentiating spin-state equilibria. Moreover, the thermal response of **1** is completely reversible upon temperature cycling, and there is no thermal hysteresis during heating and cooling cycles, as shown for five cycles between 180 and 300 K in Figure S30. This low error margin, combined with high thermal sensitivity and excellent emission contrast, underscores the exceptional potential of this single-fluorophore ratiometric platform for visualizing dynamic SCO behavior.

CONCLUSIONS

In summary, we have developed a new Fe(II) complex **1** based on a single-fluorophore ratiometric ligand. Its thermochromic spin crossover behavior spectrally matches the dual emission bands of the ligand, enabling spin-state-dependent modulation of LE and ICT emissions. Notably, the high-spin and low-spin states exhibit opposite trends in their FRET efficiencies for the LE and ICT channels, endowing complex **1** with the characteristics of a ratiometric fluorescent thermometer accompanied by distinct fluorochromism. This opposite-direction ratiometric variation amplifies the thermometer's sensitivity, reaching 210–260 K range of $S_r > 1\%\ K^{-1}$ near $T_{1/2}$ with $S_{r\,max} = 1.35\%\ K^{-1}$ at 232 K. which is also the key to achieving a high-contrast fluorochromic signal output.

On the other hand, the relatively long FRET distance of 9.6 Å ensures that both HS and LS Fe(II) centers exhibit only moderate quenching efficiencies toward the LE and ICT emissions, which evolve in opposite directions within the ranges of 33%–5% and 4%–34%, respectively. As a result, the single-fluorophore system maintains a consistently high fluorescence quantum yield (~50%) throughout the entire spin crossover process. This *bright* ratiometric fluorescence enables complex **1** to deliver a high SNR and low resolution; and robust performance even at low concentrations (10^{-4} M), significantly outperforming sensing schemes that rely solely on the thermochromism of the spin crossover core (Figure S31).

It is well known that spincrossover materials, as stimulus-responsive molecular switches, offer intrinsic advantages for multifunctional sensing.[3] In this work, we demonstrate however that integrating spin crossover transitions with ratiometric fluorescence can markedly amplify sensing contrast and sensitivity. The operating principle of this spin crossover regulated ratiometric fluorescent thermometer (RFT) parallels that of single-fluorophore RFTs, such as D–π–A fluorophores with pronounced solvatochromism.[37] Unlike these purely intramolecular systems, complex **1** anchors the spin crossover center directly onto the single-fluorophore ratiometric ligand **L1**, thereby establishing an external thermal coupling pathway that enables efficient spin-state regulation of dual emission. This design provides a new strategy for high-performance single-fluorophore RFTs. Moreover, through molecular design of a high-emission spin-state–optical coupling system, this work enables optical read-out of single-molecule spin states, providing a new pathway to “see” molecular spins. Combined with recent related studies,[63-65] this finding lays a solid foundation for the development of optical single-molecule spin–reading technologies.

References

[1] Y. Garcia, F. Robert, A. D. Naik, G. Zhou, B. Tinant, K. Robeyns, S. Michotte, L. Piraux, Spin Transition Charted in a Fluorophore-Tagged Thermochromic Dinuclear Iron(II) Complex *J. Am. Chem. Soc.* **2011**, *133*, 15850-15853.

[2] M. K. Javed, A. Sulaiman, M. Yamashita, Z.-Y. Li, Shedding light on bifunctional luminescent spin crossover materials *Coord. Chem. Rev.* **2022**, *467*, 214625.

[3] K. Senthil Kumar, M. Ruben, Emerging trends in spin crossover (SCO) based functional materials and devices *Coord. Chem. Rev.* **2017**, *346*, 176-205.

[4] A. Bousseksou, G. Molnár, L. Salmon, W. Nicolazzi, Molecular spin crossover phenomenon: recent achievements and prospects *Chem. Soc. Rev.* **2011**, *40*, 3313-3335.

[5] Y. Guo, S. Xue, M. M. Dîrtu, Y. Garcia, A versatile iron(ii)-based colorimetric sensor for the vapor-phase detection of alcohols and toxic gases *J. Mater. Chem. C* **2018**, *6*, 3895-3900.

[6] J. Linares, E. Codjovi, Y. Garcia, Pressure and Temperature Spin Crossover Sensors with Optical Detection *Sensors* **2012**, *12*, 4479-4492.

[7] E. Kuzmann, Z. Homonnay, Z. Klencsár, R. Szalay, (57)Fe Mössbauer Spectroscopy as a Tool for Study of Spin States and Magnetic Interactions in Inorganic Chemistry *Molecules* **2021**, *26*, 1742.

[8] G. Molnár, S. Rat, L. Salmon, W. Nicolazzi, A. Bousseksou, Spin Crossover Nanomaterials: From Fundamental Concepts to Devices *Adv. Mater* **2018**, *30*, 1703862.

[9] B. Benaicha, K. Van Do, A. Yangui, N. Pittala, A. Lusson, M. Sy, G. Bouchez, H. Fourati, C. J. Gómez-García, S. Triki, K. Boukheddaden, Interplay between spin-crossover and luminescence in a multifunctional single crystal iron(ii) complex: towards a new generation of molecular sensors *Chem Sci* **2019**, *10*, 6791-6798.

[10] F.-F. Yan, W.-J. Jiang, N.-T. Yao, P.-D. Mao, L. Zhao, H.-Y. Sun, Y.-S. Meng, T. Liu, Manipulating fluorescence by photo-switched spin-state conversions in an iron(II)-based SCO-MOF *Chem.Sci.* **2023**, *14*, 6936-6942.

[11] O. Kraieva, I. Suleimanov, G. Molnár, L. Salmon, A. Bousseksou, CdTe Quantum Dot Fluorescence Modulation by Spin Crossover *Magnetochemistry* **2016**, *2,* 11.

[12] G.-H. Zhao, S.-H. Zhang, C. Yi, T. Liu, Y.-S. Meng, Construction of spin crossover-fluorescence bifunctional iron(ii) complexes with modified bis(pyrazole)pyridine ligands *New J. Chem.* **2023**, *47*, 10967-10972.

[13] K. Ridier, A. Hoblos, S. Calvez, M. Lorenc, W. Nicolazzi, S. Cobo, L. Salmon, L. Routaboul, G. Molnár, A. Bousseksou, Optical properties and photonic applications of molecular spin-crossover materials *Coord.Chem.Rev.* **2025**, *535*, 216628.

[14] C. Yi, D. Chen, S.-H. Zhang, R. Cai, C. Duan, Y.-S. Meng, T. Liu, Spin-modulated near-infrared-I emission in a xanthene-decorated Fe(II) spin-crossover complex *Sci. China Chem.* **2025**, *68*, 2987-2994.

[15] B. Benaicha, K. Van Do, A. Yangui, N. Pittala, A. Lusson, M. Sy, G. Bouchez, H. Fourati, C. J. Gómez-García, S. Triki, K. Boukheddaden, Interplay between spin-crossover and luminescence in a multifunctional single crystal iron(ii) complex: towards a new generation of molecular sensors *Chem.Sci.* **2019**, *10*, 6791-6798.

[16] J. Feng, X. Wang, L. Wang, J. Kfoury, J. Oláh, S. Zhang, L. Zou, Y. Guo, S. Xue, Naphthalimide-Tagged Iron(II) Spin Crossover Complex with Synergy of Ratiometric Fluorescence for Thermosensing *Inorg.Chem.* **2024**, *63*, 108-116.

[17] N. Deorukhkar, C. Egger, L. Guénée, C. Besnard, C. Piguet, Detecting Fe(II) Spin-Crossover by Modulation of Appended Eu(III) Luminescence in a Single Molecule *J.Am.Chem.Soc.* **2024**, *146*, 308-318.

[18] N. Deorukhkar, C. Egger, A. Rosspeintner, C. Piguet, Unravelling Kinetics of Intramolecular NdIII → FeII Energy Transfer in Spin Crossover Single Molecules: Dotting the i's and Crossing the t's *J.Am.Chem.Soc.* **2024**, *146*, 19386-19396.

[19] J.-L. Wang, Q. Liu, Y.-S. Meng, X. Liu, H. Zheng, Q. Shi, C.-Y. Duan, T. Liu, Fluorescence modulation via photoinduced spin crossover switched energy transfer from fluorophores to FeII ions *Chem.Sci.* **2018**, *9*, 2892-2897.

[20] T. Lathion, N. Deorukhkar, C. Egger, H. Nozary, C. Piguet, Molecular Fe(ii)–Ln(iii) dyads for luminescence reading of spin-state equilibria at the molecular level *Dalton Trans.* **2024**, *53*, 17756-17765.

[21] T. Lathion, A. Fürstenberg, C. Besnard, A. Hauser, A. Bousseksou, C. Piguet, Monitoring Fe(II) Spin-State Equilibria via Eu(III) Luminescence in Molecular Complexes: Dream or Reality? *Inorg.Chem.* **2020**, *59*, 1091-1103.

[22] C. Yi, S.-H. Zhang, L. Zhao, N.-T. Yao, G.-H. Zhao, Y.-S. Meng, T. Liu, Constructing spin crossover-fluorescence bifunctional iron(<scp>ii</scp>) complexes based on tetraphenyl ethylene-decorated AIEgens *Dalton Trans.* **2023**, *52*, 5169-5175.

[23] J. Yuan, S. Q. Wu, M. J. Liu, O. Sato, H. Z. Kou, Rhodamine 6G-Labeled Pyridyl Aroylhydrazone Fe(II) Complex Exhibiting Synergetic Spin Crossover and Fluorescence *J.Am.Chem.Soc.* **2018**, *140*, 9426-9433.

[24] D. A. Hopper, H. J. Shulevitz, L. C. Bassett, Spin Readout Techniques of the Nitrogen-Vacancy Center in Diamond *Micromachines* **2018**, *9*(9), 437.

[25] A. Bednarkiewicz, L. Marciniak, L. D. Carlos, D. Jaque, Standardizing luminescence nanothermometry for biomedical applications *Nanoscale* **2020**, *12*, 14405-14421.

[26] A. Bednarkiewicz, J. Drabik, K. Trejgis, D. Jaque, E. Ximendes, L. Marciniak, Luminescence based temperature bio-imaging: Status, challenges, and perspectives *Applied Physics Reviews* **2021**, *8*, 011317.

[27] G. Feng, H. Zhang, X. Zhu, J. Zhang, J. Fang, Fluorescence thermometers: intermediation of fundamental temperature and light *Biomater. Sci.* **2022**, *10*, 1855-1882.

[28] Q. Ma, S. Xu, Z. Zhai, K. Wang, X. Liu, H. Xiao, S. Zhuo, Y. Liu, Recent Progress of Small-Molecule Ratiometric Fluorescent Probes for Peroxynitrite in Biological Systems *Chem. Eur. J.* **2022**, *28*, e202200828.

[29] R. Chowdhury, P. Murto, N. A. Panjwani, Y. Sun, P. Ghosh, Y. Boeije, C. D. Cordeiro, V. Derkach, S.-J. Woo, O. Millington, D. G. Congrave, Y. Fu, T. B. E. Mustafa, M. Monteverde, J. Cerdá, G. Londi, J. Behrends, A. Rao, D. Beljonne, A. Chepelianskii, H. Bronstein, R. H. Friend, Bright triplet and bright charge-separated singlet excitons in organic diradicals enable optical read-out and writing of spin states *Nat.Chem.* **2025**, *17*, 1410-1417.

[30] X. Yang, C. Li, P. Li, Q. Fu, Ratiometric optical probes for biosensing *Theranostics* **2023**, *13*, 2632-2656.

[31] X. Huang, J. Song, B. C. Yung, X. Huang, Y. Xiong, X. Chen, Ratiometric optical nanoprobes enable accurate molecular detection and imaging *Chem. Soc. Rev.* **2018**, *47*, 2873-2920.

[32] B. Sk, S. Khodia, A. Patra, T and V-shaped donor–acceptor–donor molecules involving pyridoquinoxaline: large Stokes shift, environment-sensitive tunable emission and temperature-induced fluorochromism *Chem. Commun.* **2018**, *54*, 1786-1789.

[33] Y. Ma, X. Zhou, J. Wu, Z. Dong, L. Cui, Y. Wang, A. Meijerink, Luminescence Thermometry via Multiparameter Sensing in YV1–xPxO4:Eu3+, Er3+ *J.Am.Chem.Soc.* **2025**, *147*, 12925-12936.

[34] K. E. McNeel, N. Siraj, N. Bhattarai, I. M. Warner, Fluorescence-Based Ratiometric Nanosensor for Selective Imaging of Cancer Cells *ACS Omega* **2019**, *4*, 1592-1600.

[35] F. Zheng, Y. Ma, J. Ding, S. Huang, S. Zhang, X. Huang, B. Feng, H. Zeng, F. Chen, W. Zeng, Ratiometric and discriminative visualization of autophagic processes with a novel dual-responded lysosome-specific fluorescent probe *Biomater. Res.* **2023**, *27*, 66.

[36] M. K. Goshisht, N. Tripathi, G. K. Patra, M. Chaskar, Organelle-targeting ratiometric fluorescent probes: design principles, detection mechanisms, bio-applications, and challenges *Chem.Sci.* **2023**, *14*, 5842-5871.

[37] A. Hori, A. Matsumoto, J. Ikenouchi, G.-i. Konishi, D−π–A Fluorophores with Strong Solvatochromism for Single-Molecule Ratiometric Thermometers *J.Am.Chem.Soc.* **2025**, *147*, 9953-9961.

[38] D.-H. Liu, Z.-B. Sun, Z.-H. Zhao, Q. Peng, C.-H. Zhao, 1,1′-Binaphthyl Consisting of Two Donor–π–Acceptor Subunits: A General Skeleton for Temperature-Dependent Dual Fluorescence *Chem. Eur. J.* **2019**, *25*, 10179-10187.

[39] H. Naito, K. Nishino, Y. Morisaki, K. Tanaka, Y. Chujo, Solid-State Emission of the Anthracene-o-Carborane Dyad from the Twisted-Intramolecular Charge Transfer in the Crystalline State *Angew. Chem. Int. Ed.* **2017**, *56*, 254-259.

[40] J. Feng, K. Tian, D. Hu, S. Wang, S. Li, Y. Zeng, Y. Li, G. Yang, A Triarylboron-Based Fluorescent Thermometer: Sensitive Over a Wide Temperature Range *Angew. Chem. Int. Ed.* **2011**, *50*, 8072-8076.

[41] S. Sasaki, G. P. C. Drummen, G.-i. Konishi, Recent advances in twisted intramolecular charge transfer (TICT) fluorescence and related phenomena in materials chemistry *J.Mater.Chem.C* **2016**, *4*, 2731-2743.

[42] Z. Zhang, G. Sun, W. Chen, J. Su, H. Tian, The endeavor of vibration-induced emission (VIE) for dynamic emissions *Chem.Sci.* **2020**, *11*, 7525-7537.

[43] W. Song, W. Ye, L. Shi, J. Huang, Z. Zhang, J. Mei, J. Su, H. Tian, Smart molecular butterfly: an ultra-sensitive and range-tunable ratiometric thermometer based on dihydrophenazines *Mater. Horiz* **2020**, *7*, 615-623.

[44] L. Shi, W. Song, C. Lian, W. Chen, J. Mei, J. Su, H. Liu, H. Tian, Dual-Emitting Dihydrophenazines for Highly Sensitive and Ratiometric Thermometry over a Wide

Temperature Range *Adv. Opt. Mater.* **2018**, *6*, 1800190.

[45] H. E. Mason, W. Li, M. A. Carpenter, M. L. Hamilton, J. A. K. Howard, H. A. Sparkes, Structural and spectroscopic characterisation of the spin crossover in [Fe(abpt)2(NCS)2] polymorph A *New J. Chem.* **2016**, *40*, 2466-2478.

[46] A. B. Gaspar, M. Carmen Muñoz, N. Moliner, V. Ksenofontov, G. Levchenko, P. Gütlich, J. Antonio Real, Polymorphism and Pressure Driven Thermal Spin Crossover Phenomenon in [Fe(abpt)2(NCX)2] (X = S, and Se): Synthesis, Structure and Magnetic Properties *Mon.Chem.* **2003**, *134*, 285-294.

[47] Z. G. Lada, K. S. Andrikopoulos, A. Chrissanthopoulos, S. P. Perlepes, G. A. Voyiatzis, A Known Iron(II) Complex in Different Nanosized Particles: Variable-Temperature Raman Study of Its Spin-Crossover Behavior *Inorg.Chem.* **2019**, *58*, 5183-5195.

[48] L. Yao, S. Zhang, R. Wang, W. Li, F. Shen, B. Yang, Y. Ma, Highly Efficient Near-Infrared Organic Light-Emitting Diode Based on a Butterfly-Shaped Donor–Acceptor Chromophore with Strong Solid-State Fluorescence and a Large Proportion of Radiative Excitons *Angew. Chem. Int. Ed.* **2014**, *53*, 2119-2123.

[49] N. Mataga, Y. Kaifu, M. Koizumi, Solvent Effects upon Fluorescence Spectra and the Dipolemoments of Excited Molecules *Bull. Chem. Soc. Jpn.* **1956**, *29*, 465-470.

[50] L. Long, X. Li, D. Zhang, S. Meng, J. Zhang, X. Sun, C. Zhang, L. Zhou, L. Wang, Amino-coumarin based fluorescence ratiometric sensors for acidic pH and their application for living cells imaging *RSC Adv.* **2013**, *3*, 12204-12209.

[51] A. Demeter, S. I. Druzhinin, S. A. Kovalenko, T. A. Senyushkina, K. A. Zachariasse, Dual Fluorescence and Ultrafast Intramolecular Charge Transfer with 6-N,N-Dialkylaminopurines. A Two-State Model *J. Phys. Chem. A* **2011**, *115*, 1521-1537.

[52] S. I. Druzhinin, N. P. Ernsting, S. A. Kovalenko, L. P. Lustres, T. A. Senyushkina, K. A. Zachariasse, Dynamics of Ultrafast Intramolecular Charge Transfer with 4-(Dimethylamino)benzonitrile in Acetonitrile *J. Phys. Chem. A* **2006**, *110*, 2955-2969.

[53] M. A. Halcrow, Structure:function relationships in molecular spin-crossover complexes *Chem. Soc. Rev.* **2011**, *40*, 4119-4142.

[54] G. J. Long, Spin Crossover in Transition Metal Compounds III. Topics in Current Chemistry, 235 Edited by Philipp Gütlich (Johannes Gutenberg-Universität, Mainz) and Harold A. Goodwin (University of New South Wales). Springer-Verlag: Berlin, Heidelberg. 2004. *J.Am.Chem.Soc.* **2005**, *127*, 4540-4540.

[55] E. M. Schubert, Utilizing the Evans method with a superconducting NMR spectrometer in the undergraduate laboratory *J. Chem. Educ.* **1992**, *69*, 62.

[56] Y. Guo, A. Rotaru, H. Müller-Bunz, G. G. Morgan, S. Zhang, S. Xue, Y. Garcia, Auxiliary alkyl chain modulated spin crossover behaviour of [Fe(H2Bpz2)2(Cn-bipy)] complexes *Dalton Trans.* **2021**, *50*, 12835-12842.

[57] P. A. Tanner, L. Zhou, C. Duan, K.-L. Wong, Misconceptions in electronic energy transfer: bridging the gap between chemistry and physics *Chem. Soc. Rev.* **2018**, *47*, 5234-5265.

[58] J. S. Lindsey, M. Taniguchi, D. F. Bocian, D. Holten, The fluorescence quantum yield parameter in Förster resonance energy transfer (FRET)—Meaning, misperception, and molecular design *Chem. Phys. Rev.* **2021**, *2*, 011302.

[59] S. E. Braslavsky, E. Fron, H. B. Rodríguez, E. S. Román, G. D. Scholes, G. Schweitzer, B. Valeur, J. Wirz, Pitfalls and limitations in the practical use of Förster's theory of resonance energy transfer *Photoch. Photobio. Sci.* **2008**, *7*, 1444-1448.

[60] P. Gütlich, Y. Garcia, H. A. Goodwin, Spin crossover phenomena in Fe(II) complexes *Chem. Soc. Rev.* **2000**, *29*, 419-427.

[61] T. K. Ekanayaka, K. P. Maity, B. Doudin, P. A. Dowben, Dynamics of Spin Crossover Molecular Complexes *Nanomaterials (Basel, Switzerland)* **2022**, *12*(10), 1742.

[62] S. Decurtins, P. Gütlich, C. P. Köhler, H. Spiering, A. Hauser, Light-induced excited spin state trapping in a transition-metal complex: The hexa-1-propyltetrazole-iron (II) tetrafluoroborate spin-crossover system *Chem. Phys. Lett.* **1984**, *105*, 1-4.

[63] A. Mizuno, R. Matsuoka, S. Kimura, K. Ochiai, T. Kusamoto, Spin-Correlated Luminescence of a Carbazole-Containing Diradical Emitter: Single-Molecule Magnetoluminescence and Thermally Activated Emission *J.Am.Chem.Soc.* **2024**, *146*, 18470-18483.

[64] S. M. Kopp, S. Nakamura, B. T. Phelan, Y. R. Poh, S. B. Tyndall, P. J. Brown, Y. Huang, J. Yuen-Zhou, M. D. Krzyaniak, M. R. Wasielewski, Luminescent Organic Triplet Diradicals as Optically Addressable Molecular Qubits *J.Am.Chem.Soc.* **2024**, *146*, 27935-27945.

[65] R. Matsuoka, S. Kimura, T. Miura, T. Ikoma, T. Kusamoto, Single-Molecule Magnetoluminescence from a Spatially Confined Persistent Diradical Emitter *J.Am.Chem.Soc.* **2023**, *145*, 13615-1362

TOC

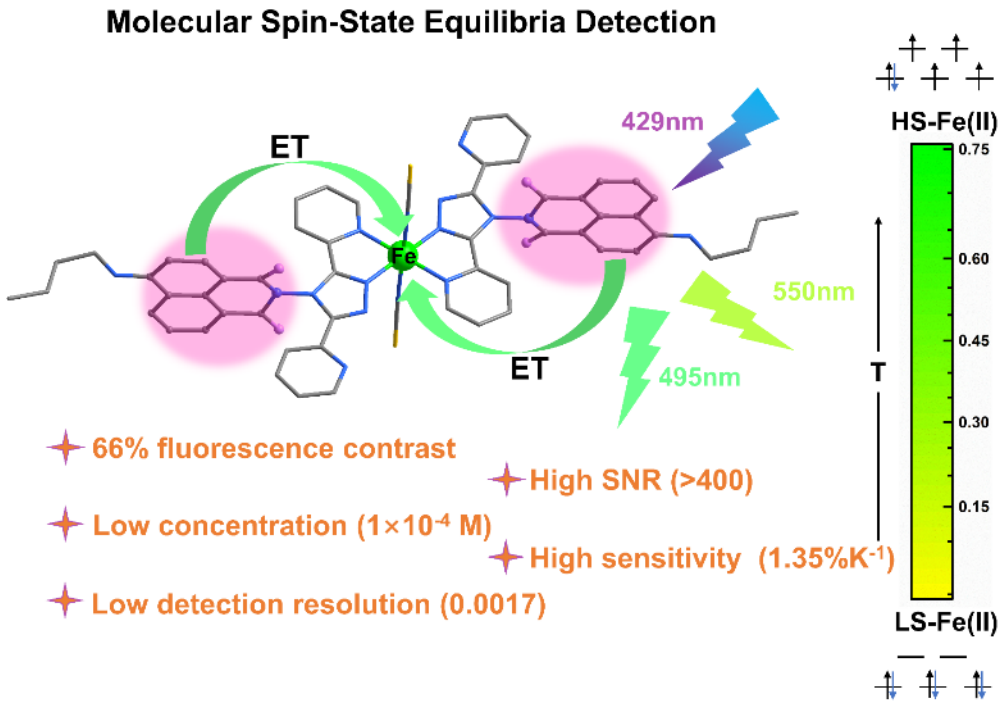
Molecular Spin-State Equilibria Detection
ET
Fe
ET
429nm
550nm
495nm
66% fluorescence contrast
High SNR (>400)
Low concentration (1×10-4 M)
High sensitivity (1.35%K-1)
Low detection resolution (0.0017)
HS-Fe(II)
0.75
0.60
0.45
0.30
0.15
T
LS-Fe(II)